

ELEMENTAL COMPOSITION FROM GAMMA-RAY SPECTROSCOPY OF THE NEAR-SHOEMAKER LANDING SITE ON 433 EROS

Larry G. Evans^{1*}, Richard D. Starr², Johannes Brückner³, Robert C. Reedy⁴,
William V. Boynton⁵, Jacob I. Trombka⁶, John O. Goldsten⁷, Jozef Masarik^{3,8},
Larry R. Nittler^{6,9}, and Timothy J. McCoy¹⁰

¹Science Programs, Computer Sciences Corporation, Lanham-Seabrook, MD 20706 USA

²Physics Department, Catholic University of America, Washington, DC 20064 USA

³Max-Planck-Institut für Chemie, D-55020 Mainz, Germany

⁴MS-D436, Los Alamos National Laboratory, Los Alamos, NM 87545 USA

⁵Lunar and Planetary Laboratory, University of Arizona, Tucson, AZ 85721 USA

⁶Laboratory for Extraterrestrial Physics, NASA Goddard Space Flight Center, Greenbelt, MD
20771 USA

⁷Applied Physics Laboratory, Johns Hopkins University, Laurel, MD 20723

⁸Present Address: Department of Physics, Komensky University, Mlynska dolina F/1,
Sk-842 48 Bratislava, Slovakia

⁹Present Address: Department of Terrestrial Magnetism, Carnegie Institution of Washington,
Washington DC 20015 USA

¹⁰Department of Mineral Sciences, National Museum of Natural History
Smithsonian Institution, Washington DC 20560 USA

*Correspondence author's e-mail address: larry.evans@gsfc.nasa.gov

Submitted to Meteoritics and Planetary Science, August 3, 2001.

Revision submitted: October 3, 2001.

ABSTRACT – Elemental composition and composition ratios derived from gamma-ray measurements collected by the NEAR-Shoemaker spacecraft while on the surface of 433 Eros are reported. Performance of the gamma-ray spectrometer (GRS) during cruise and orbit is reviewed. The best gamma-ray data were collected on the surface of Eros after the spacecraft's controlled descent on 12 February 2001. Methods used in spectral analysis, to convert peak areas to incident photons, and photons to elemental composition are described in some detail. The elemental abundance of K and the Mg/Si, Fe/Si, Si/O and Fe/O abundance ratios were determined. The Mg/Si and Si/O ratios and the K abundance are roughly chondritic, but the Fe/Si and Fe/O ratios are low compared to expected chondritic values. Three possible explanations for the apparent Fe depletion are considered.

INTRODUCTION

In February 1996, the Near Earth Asteroid Rendezvous (NEAR-Shoemaker) mission was launched into space on a planned three-year cruise to the near-Earth asteroid, 433 Eros. The NEAR spacecraft, the first in the Discovery program to be launched, was built by the Johns Hopkins University, Applied Physics Laboratory (APL). The spacecraft was designed to orbit Eros for one year and carried a group of remote sensing instruments including X-ray and gamma-ray spectrometers (XGRS) to measure elemental composition (Trombka et al., 1997). Due to a problem with firing of the main rocket engine in December 1998, the rendezvous was delayed until February 2000. The NEAR spacecraft was the first spacecraft to orbit a body as small as Eros, which is about 33 km X 13 km X 13 km.

Reflectance spectroscopy of 433 Eros indicates that it is an S-type asteroid, the most common type in the inner main belt and the near-Earth population. The S asteroids are an agglomeration of bodies with different geologic histories, ranging from primitive, chondritic bodies to partially-differentiated asteroids (Gaffey et al., 1993). While the linkage between this range of geologic processes and S-type asteroids appears solid, deciphering the history of any particular S asteroid has been difficult. Further, it has been impossible to link specific meteorites, which are known to be samples of asteroids, with specific asteroids. As the most common type of asteroid in the inner belt, many authors have argued that S asteroids should be parental to ordinary chondrites, the most common type of meteorite falling to Earth today (Wetherill, 1985). One of the prime mission objectives was to obtain the elemental composition of 433 Eros. This determination, with sufficient accuracy to allow comparison with major meteorite types, would significantly enhance our ability to make asteroid-meteorite linkages.

The selection of an X-ray spectrometer (XRS) and a gamma-ray spectrometer (GRS) for this mission was based on their ability to determine spatially-resolved elemental composition of the asteroid. XRS measurements were expected to give elemental composition results for Mg, Al, and Si, and depending on composition and solar conditions, results for S, Ca, Ti and Fe. Gamma-ray measurements can determine the abundance of elements such as O, Si, Fe, Ca, Ti, Mg, H, K, Th, and U depending on the actual composition. Results for the XRS and GRS overlap in determining the composition of elements such as Mg, Si, and Fe. However, the results are complementary in that the GRS measures composition down to depths of 10s of cm with very broad spatial resolution while the XRS results are for a thin layer of surface material and better spatial resolution than the GRS.

An early orbit plan (October 1996) for the mission had scheduled some 158 days of orbit at or below 35 km from the asteroid center-of-mass including 67 days at 25 km orbit. It was known, that the asteroid would not fill the field-of-view (FOV) of the GRS even at that lowest altitude where the average solid angle was about half the FOV. Thus, it was important to accumulate as much time as possible at low altitudes to achieve the desired uncertainty in the GRS results. However, the late arrival at Eros and operational considerations required the orbital plan to be changed so that less than 60 days of orbit at 35 km could be achieved.

GAMMA-RAY SPECTROMETER

Gamma-ray photons in the energy region 0.1-10 MeV are emitted by excited nuclei and have discrete energies characteristic of that element. The excitation of nuclei can come from the radioactive decay of very-long-lived radioisotopes in planetary materials, such as ^{40}K , ^{238}U , and ^{232}Th . For other elements in space, excitation is provided by cosmic-ray bombardment. Except for periods of time during and immediately after major solar particle events, this excitation is caused mainly by galactic cosmic rays (GCR) (Evans et al., 1993).

GCR are nuclear particles, mainly protons and helium nuclei (alpha particles), with a broad range in energy, (typically of order a GeV) and a nearly isotropic flux of about 2-3 particles/(cm²-s). These particles generate nuclear cascades on striking dense matter. The cascade particles most effective in generating gamma rays are neutrons. The high-energy neutrons produced in this manner can undergo further nuclear collisions. They may excite stable nuclei to higher energy levels by inelastic scatter. The resulting de-excitation of the nucleus can result in the emission of a gamma ray and is termed an inelastic scatter reaction; (n,n' γ). Neutrons may also lose energy by elastic scatter until their energy is comparable to the thermal energy of a nucleus at a given temperature. These thermal neutrons can be captured by a nucleus and the resulting decay to the ground state of this new isotope, can produce a capture gamma ray; (n, γ). The intensity of gamma rays emitted by a particular element and for a particular process depends on the concentration of that element, the reaction cross-section for the process, and the number of neutrons available with the appropriate energy. The inelastic scatter reactions have a large cross section for all common nuclei at energies above the reaction threshold energy. Therefore, all the most abundant elements give a useful yield of gamma rays from this process. Thermal neutron cross sections vary by orders-of-magnitude, and yields for neutron capture gamma rays for the most abundant elements also vary widely (Evans et al., 1993). Material containing large concentrations of elements with large neutron capture cross-sections can alter the thermal flux and can lead to a flux depression of neutron capture gamma-rays (Reedy, 1978).

The neutron cascade penetrates into a planetary surface to a depth of hundreds of g/cm², a few meters into the regolith on an object like an asteroid with no atmosphere. Gamma rays are scattered (with loss of characteristic energy) or absorbed on a distance scale of tens of g/cm². This indicates that only those gamma rays generated in the first tens of g/cm² can be identified on the surface or from orbit, and the important part of the neutron equilibrium distribution in the planetary body is that near the surface. The moderation and thermalization of the neutrons depend strongly on the composition of the near surface material, particularly on the hydrogen and carbon content, if any. Gamma-ray detectors on the surface or in an orbiting spacecraft can measure the discrete energy gamma rays and determine the elements that emitted these gamma rays (Boynton et al., 1992, Boynton et al., 1993, Trombka et al., 1997).

Besides the characteristic gamma rays emerging from the asteroid surface, there will be a number of other sources of gamma rays that will be a background from which the gamma rays of interest will have to be separated. Some of these sources of background produce discrete lines and some appear as part of a continuum. Based on previous spaceflight experience, the major background components measured in orbit are: partial energy deposition in the detector (Compton effect), cosmic-ray activation of the detector and materials surrounding the detector;

characteristic gamma rays emitted from the surface material, but scattered before emerging from the asteroid; cosmic-ray activation and natural radioactivity in the spacecraft; and gamma emission from astrophysical sources (Bielefeld et al., 1976).

Most current gamma-ray detectors utilize either inorganic scintillation material, such as sodium iodide (NaI) or bismuth germanate (BGO), or semiconductor material, such as high-purity germanium (Ge). The Ge detectors have significantly better energy resolution than scintillation detectors and are generally favored for laboratory measurements. For example, the typical energy resolution (expressed as the full-width at half-maximum, FWHM, of the peak) for a Ge detector is 2 keV measured at 1332 keV from a ^{60}Co calibration source. A similar FWHM for a NaI detector is 80 keV at 1332 keV. In addition, the Ge detector has a much better peak-to-Compton ratio, typically about 50 compared to 2 for a NaI detector (Knoll, 1989). These two factors give a Ge detector a decided advantage in resolving peaks close in energy and detecting peaks in the presence of significant continuum.

While Ge detectors improve detection capability, they also require operation at cryogenic temperatures (typically <100 K) and suffer serious degradation in performance when exposed to cosmic radiation over long periods of time (Brückner et al., 1991). Typically Ge detectors on planetary missions (such as Mars Odyssey 2001) are designed with anneal capability to offset the expected resolution degradation during spaceflight. These limitations of a Ge detector along with the added cost and complexity reduced some of the advantages that might be expected for a space mission. Analysis during the preliminary design phase of the NEAR mission indicated that a scintillation detector could meet the science objectives of the mission (Evans et al., 1995). Experience in both U.S. and Russian planetary missions and in the oil well-logging industry have shown that good results could be obtained using scintillation detectors for such elements as K, Th, O, H, Mg, Si, Ti, and Fe. In addition, proposed design changes were expected to improve detector performance over scintillators that have previously flown in space. NaI was chosen as the scintillator for NEAR because it has the best energy resolution of common scintillation materials in combination with a photomultiplier tube (PMT). These systems are rugged and have been used successfully on space flight missions for many years (Evans et al., 1993).

The pulse height spectrum obtained when monoenergetic gamma rays are detected has a shape determined by the gamma-ray energy and the characteristics of the detector. Important factors are (1) the relative magnitude of the photoelectric, Compton, and pair-production cross-sections as a function of energy, and (2) the statistical fluctuations and losses involved in collecting the signal generated in the detector (Knoll, 1989). A measurement reflects the amount of energy that is lost in the detector and transferred as kinetic energy to electrons. At energies where the photoelectric absorption dominates, the kinetic energy imparted to a secondary electron is equal to the gamma-ray energy minus the electron binding energy. This energy can be reclaimed, in a sense, by the absorption of the X-rays produced by photoelectric absorption. At higher energies, when Compton scattering becomes more important, the gamma ray may lose part of its energy to the detector and escape the crystal or may then be photo absorbed. The gamma ray will lose all or part of its energy in the detector and possibly escape with diminished energy. This generates a continuum that adds to the background up to the energy of the initial gamma ray minus the minimum scattered energy.

At energies above 1022 keV, electron-positron pair production becomes possible. The electron produced will eventually lose all its kinetic energy in the detector while the positron will annihilate with another electron producing two 511 keV photons. The energy of these photons can either be absorbed in the detector or can escape. Therefore, three peaks will be created (1) pair production with eventual absorption of both 511 keV photons to give a peak at the initial gamma-ray energy, (2) pair production with the absorption of one 511 photon and the escape of the other giving a peak at the initial gamma-ray energy minus 511 keV, and (3) pair production with the escape of both 511 keV photons giving a peak at the initial gamma-ray energy minus 1022 keV.

Cosmic-ray interactions in the spacecraft produce gamma-rays characteristic of the spacecraft materials. These gamma rays constitute an unwanted background signal that could degrade the science return of the mission. Gamma-ray detectors of previous missions have often used a boom to move the gamma-ray detector away from the spacecraft, reducing substantially the spacecraft background. On Mars Odyssey, for example, the gamma-ray detector is mounted on a boom that can be extended to 6 meters from the spacecraft. The NEAR detector had to be body mounted on the lower deck along with all the other instruments. This required some other method of reducing the spacecraft background.

Plastic scintillators are very effective charged-particle shields, but higher density materials are needed to shield gamma rays. Passive shielding is not practical because of the large volume and mass of material needed to absorb the cosmic rays and the secondary radioactive products produced in the shield. An active collimator is used to reduce the charged particle, spacecraft and cosmic gamma-ray backgrounds as well as the Compton continuum. Charged particles or photons that interact in the shield produce a corresponding output signal. This signal can be used to trigger an anti-coincidence system to reject any counts in the central detector that are in coincidence with the shield within some time window. BGO (bismuth germinate, $\text{Bi}_4\text{Ge}_3\text{O}_{12}$) was chosen for the NEAR shield. It has a density of 7.13 g/cm^3 , which makes it especially effective for gamma ray interactions. However, the presence of a large mass of BGO near the central detector has some negative aspects due to possible activation of the BGO by GCR.

As useful as the NEAR shield would be to reduce the detector background, significant information on the gamma-ray flux from the asteroid would be lost if only the anticoincidence spectrum was collected. The first and second escape peaks produced in the central detector will be mostly eliminated in the anti-coincidence spectrum. For a small central detector like the NEAR design, this loss would be unacceptable since the escape peaks would have many more counts than the full-energy peak for many energies of interest. For example, at 6 MeV, calculations indicate that 85% of all the counts would be in the escape peaks and only 15% in the full-energy peak. The NEAR design recovers these peaks with two additional NaI spectra; one in coincidence with 511 keV and one in coincidence with 1022 keV energy deposition in the BGO shield. Calibrations with the NEAR detector indicate the effectiveness of this design for reducing the continuum and capturing the escape peaks (Evans et al., 2000).

A radioactive source for energy calibration was not included in the NEAR design. It was expected that enough discrete lines from background sources would be measured in the spectra that the energy calibration could be monitored. The strongest of these would be the 511 keV line

due to electron/positron annihilation in the spacecraft and materials surrounding the detector. Other gamma rays from cosmic-ray interactions in the scintillation materials would be expected. Measurements taken during the cruise portion of the mission confirmed these predictions and will be discussed below.

A description of the GRS detection scheme is given in Goldsten et al., 1997 and will be briefly summarized here. An incoming photon is absorbed by the detector material and produces an output signal proportional to the energy absorbed. The detector signal is amplified, filtered, and its peak value measured using an analog-to-digital converter. A data processor collects the measurements and bins them according to the energy absorbed into a pulse-height spectrum. Five 1024-channel spectra are collected simultaneously. These are: the NaI raw spectrum, with no coincidence or anti-coincidence rejection; the BGO raw spectrum; the NaI spectrum measured in anti-coincidence with the BGO; the NaI spectrum measured in coincidence within a window around 511 keV in the BGO detector; the NaI spectrum measured in coincidence within a window around 1022 keV in the BGO detector. In addition two 21-channel spectra are collected from the BGO detector in coincidence with the NaI and in the windows specified around the 511 keV and 1022 keV energies.

Temperature and voltage stability are extremely important to maintain system performance. The light outputs of the NaI and BGO detectors vary significantly with temperature. The detectors are thermally isolated and wrapped with operational heaters to stabilize the temperature to within 0.25° C. The signal gains of the PMTs are not particularly sensitive to temperature, but are very sensitive to voltage variations. The XGRS uses an external feedback control system to produce ultra-stable high-voltage outputs from the onboard high-voltage power supplies (Goldsten et al., 1997). No gain changes due to temperature or high-voltage variation were observed during the mission.

ORBITAL MEASUREMENTS

The GRS was turned on a number of times during the four-year cruise period. Long term background measurements were accumulated and analyzed. Numerous gamma-ray peaks from activation of the central detector, of the BGO shield, and of material in the spacecraft were observed and tentatively identified. This information is important as count rates measured while in orbit around Eros have to be corrected for these background counts. A major change observed during the cruise phase of the mission was that the gamma-ray count rate decreased significantly starting sometime in 1999. The general background was fairly constant from 1996 to 1998 but decrease by about a factor of 2 when measured in May-June 1999. Subsequent measurements in January 2000 before the spacecraft entered an orbit around Eros, showed a further reduction of a factor of 1.5. The GCR flux decreases around the time of solar maximum due to the high solar activity and the stronger magnetic fields carried by the solar wind.

Tentative identifications of gamma-ray peaks analyzed in the cruise data were reported in Dyer et al. (1998). Unfortunately, many of these peaks are at the same energies of lines expected from Eros and a careful analysis of the orbital data is required to prevent gamma rays identified in the spectra to be attributed to Eros that actually come from the background. The most prominent line identified in the background spectra is at 2.6 MeV and is due to activation of bismuth in the

shield. This is the same energy usually used to identify Th from a planetary body.. The gamma ray at 2.614 MeV from Th comes from the daughter product ^{208}Tl and is the strongest line in the Th decay chain (Reedy, 1978). The background activation line comes from ^{209}Bi that can produce ^{208}Tl or excited ^{208}Pb by a number of different mechanisms. A complete understanding of the energy and magnitude of these background emissions will be necessary in order to fully analyze the low-altitude orbital data.

The first chance to make GRS measurements from the 35 km orbit occurred in July 2000. The spacecraft entered the 35 km orbit on July 14, 2000, for 10 days. On that same day a very large solar particle event occurred on the sun that resulted in a large flux of charged particles hitting the GRS a short time later. The flux of charged particles was large enough to cause the detector to enter a safe mode (as it was designed to do). It was not until July 18 that the detector was turned on again. Inspection of the GRS spectra from that day through the rest of the 35 km orbital period showed strong activation of the detector materials. **Fig. 1** shows spectra of the detector both before the solar particle event and two days following the turn on. Because of this high background, no useable asteroid data were obtained during the July 2000 35 km orbit.

The spacecraft again entered a 35 km orbit near the end of the mission in December 2000. During much of the next 6 weeks asteroid data were collected by the GRS. The average solid angle of the asteroid made with the GRS was about 0.2 steradians compared to the field-of-view (FOV) of the detector of about 0.6 steradians. Corrections to the spectra taken with the asteroid in the FOV are needed to reduce the background from the spacecraft and the local materials. Two possible means of correcting the spectra for the background were investigated; using the spectra taken with the asteroid not in the FOV (FOV=0), but close in time to spectra taken with the asteroid in the FOV or spectra taken in the high altitude orbit where the solid angle of the asteroid was very small. It was determined that the latter method was better, as the BGO shield in the FOV=0 case was less effective as a shield for higher energy gamma rays (e.g., >3 MeV) that were of great interest for analysis.

Examples of spectra taken during the 35 km orbit while the GRS was pointed at the asteroid are shown in **Figs. 2** and **3** for the anticoincidence and second escape spectra, respectively. These spectra were taken during December 2000 and January 2001 and represent an accumulation time of about 24 days. Also shown are spectra taken during the 200 km orbit in November and December 2000 with about 17 days accumulation. The spectra are time normalized and the difference between the 35 km spectrum and the 200 km spectrum are shown in both a log plot and a linear plot. It can be seen that the difference spectrum in each case contains little structure that would indicate a strong gamma-ray peak. Gamma-ray lines that should be the strongest from the asteroid, such as the 6.129 MeV line from oxygen, do not show up in the difference spectra. This seems to indicate that the spectrum, whether near or far from the asteroid, is dominated by the local material and spacecraft backgrounds which were higher than expected. The combination of a small central detector and the mounting directly on the spacecraft gave a signal to continuum ratio that was too small for the required sensitivity. A discussion of this signal to noise problem for the NEAR GRS is given in Trombka et al, 2000. Accumulations for longer time periods did not change this result. It is possible that refinements on data accumulation by, for example, summing spectra with the same GCR fluxes or by a more systematic analysis of the background, might improve this situation. However, so far, no strong

discrete line gamma rays that are unambiguously from the asteroid have been identified. Fortunately, an unexpected opportunity presented itself that gave a gamma-ray signal that was definitely from the asteroid.

SURFACE MEASUREMENTS

At the end of the one year orbit of NEAR around Eros, it was decided to attempt a controlled descent to the surface of the asteroid. The principal goal was to obtain extremely high-resolution images of the surface as the spacecraft descended. After a dramatic descent to the surface, telemetry ceased, but indications were that the spacecraft had survived the landing. Based on the final high-resolution images, the spacecraft appears to have landed (Veverka et al., 2001b) inside a small crater with a “pond” (Veverka et al., 2001a) of smooth, fine material. NASA decided to extend the mission for another two weeks and allow the GRS to accumulate data while sitting on the surface. Subsequent analysis indicated that the GRS was pointed toward the surface, about 18 degrees from the normal to the surface.

The fixed high-gain antenna on the spacecraft was not pointed towards the Earth so the omnidirectional low gain antenna had to be used for telemetry. This severely limited telemetry rate to about 10 bits/s. Only spectra were transmitted with little engineering or ancillary data. The first two days of data were used to calibrate the detectors as the temperature had changed significantly from the orbital measurements. Adjustments to the high-voltage and thus to the energy gain were made to insure that the escape-peak spectra would be valid. After that adjustment, spectra were accumulated over the next seven days. Spectra taken with the GRS on the surface are shown in **Fig. 4**. The escape peak spectra are divided by constants for better visualization. The broad feature extending to about 2 MeV in the anticoincidence spectrum was not seen in the orbital measurements. Laboratory measurements using the engineering model of the GRS showed that this feature was due to the activation of ^{128}I (half-life of 25 minutes) in the central NaI crystal by thermal neutron capture. All the spectra shown in **Fig. 4** were corrected for differential non-linearity and the raw NaI spectrum and the BGO spectrum are corrected for roll-overs due to the long accumulation times on the surface. The NaI anticoincidence and escape spectra and the BGO spectrum form the basis of the subsequent analysis for the composition of Eros from the GRS.

In order to determine composition from the GRS data, three steps are necessary; (1) analysis of the spectra to determine peak areas, (2) conversion of the peak areas to photons using the efficiency of the detector, and (3) conversion of the photons to composition using calculations of gamma-ray production for different compositions. Each of these steps will be discussed in some detail as the method and assumptions are important to understand the results.

Spectral Analysis

The spectral analyses of the measured pulse-height spectra were carried out in an iterative procedure using calculated elemental response functions. These response functions duplicated the method used to collect the anticoincidence and escape spectra with the detector system. The calculations include the Compton continuum reduction in the anticoincidence spectra and the capture of the escape spectra with coincidences around 511 keV and 1022 keV between the

central crystal and the BGO shield. Comparisons of calculated responses with measurements taken during detector calibrations indicate that these response functions give a reasonably accurate representation of the shape of the measured responses. In the following analysis, the calculated response functions were assumed to have no uncertainty directly attributed to them compared to other uncertainties in the analysis.

A major step in the analysis is to separate the measured spectrum into a continuum and a set of discrete lines. A major area of uncertainty in the analysis is to determine accurately the continuum that underlies the discrete line spectrum as the continuum is expected to be a significant component of the total signal. On Apollo the discrete lines from the Moon represented only about 10-15% of the total signal (Bielefeld et al., 1976). The ratio of signal to continuum for the NEAR GRS should be better than for Apollo, since Apollo had no Compton suppression in the anticoincidence mode nor any escape modes.

The spectral unfolding procedure was similar for each spectrum, though each was done separately. The response of each element expected in the spectrum was used to fit the measured spectrum along with a first estimate of the continuum. The escape spectra were only used for high-energy gamma rays (> 3 MeV) as the efficiency for lower energies is small. The spectra were assumed to have an energy calibration that was linear, since the response functions were generated with that assumption. This seemed to be true for the energy range of interest in the escape spectra. The anticoincidence spectrum was analyzed in separate parts (for energies < 3 MeV and for energies > 3 MeV) as a linear energy calibration would not work over the whole spectrum. The results for the first estimate of the discrete line intensities were used to subtract from the measured spectrum, and the difference was used to calculate a new continuum by fitting a spline through the difference spectrum. This resulting spline fit was then used to subtract from the measured spectrum and the difference used to calculate the second approximation to the discrete line spectrum. The response functions were fit to the discrete line spectrum by a matrix inversion technique similar to that used in the Apollo analysis (Bielefeld et al. 1976, Trombka et al. 1979,). The iteration was carried out again and the results compared to the previous results. When the discrete lines and continuum did not change appreciably after an iteration, the procedure was terminated.

The gamma rays originating from natural radioactivity, from neutron inelastic scatter reactions, and from neutron capture reactions are each considered separately. The response functions for Fe capture, Fe inelastic, O inelastic, Si inelastic, Si capture, Mg inelastic, and ^{40}K were used in the fits. An example of a calculated response function is shown in **Fig. 5**. In addition some other monoenergetic response functions existing in the background spectra were added to the fit for each spectrum. For example, a prominent peak at 2.6 MeV is evident in the cruise, orbital, and surface spectra. Analysis of this peak in the surface spectra showed that the intensity did not change appreciably from that in the orbital spectra.

The results of the fitting procedure for the low and high energy portion of the NaI anticoincidence spectrum are shown in **Figs. 6 and 7** and for the results for escape peak spectra are shown in **Figs. 8 and 9**. The top portion of each figure has the measured spectrum, the final spline fit, and the difference spectrum. The bottom portion of each figure shows the fit of the response functions to the difference spectrum. The results of each fit are the counts in the peaks

for each element used in the fit. To convert these counts in the detector to photons incident on the detector requires knowledge of the efficiency of the detector.

GRS Efficiency

The intrinsic peak efficiency of a gamma-ray detector is defined as the number of counts in a peak per photon incident on the detector. Preflight calibrations of the NEAR GRS were made to determine the efficiency of the NaI and BGO detectors as a function of energy and angle (Evans et al. 2000). Radioactive sources ranging in energy from 320 keV to 6.129 MeV were used. In addition, a ^{252}Cf neutron source was used to irradiate H, Si, and Fe targets that produce lines at 2.223, 4.934 and 7.631+7.646 MeV, respectively. Measurements were taken at angles ranging from 0 degrees to 90 degrees with respect to the long axis of the detector. For orbital measurements the efficiency at 0 degrees is adequate to describe the response of the detector. However, on the surface of Eros the GRS detects gamma rays from the asteroid at angles up to 90 degrees, corresponding to a nearly 2π geometry. With the spacecraft resting on the surface of Eros, the angle of the GRS with respect to the surface normal was determined to be 18 degrees.

To calculate the detector response on the asteroid's surface we did a weighted average of the measured efficiencies as a function of angle and energy. The 18 degree offset from the surface normal is included, but in fact has only a small effect. Such a tilt angle would only become important if it exceeded the half-opening angle of the NaI, which is about 25 degrees.

Total efficiencies were calculated for the NaI photopeak, first escape, and second escape spectra and are shown in **Fig. 10**. The photopeak efficiency is significantly lower than that given in Evans et al. (2000) at 0 degrees, though the shapes of the curves are similar. The decrease is due to the impact of the BGO shield. As explained above, on the surface of Eros the viewing geometry is nearly 2π steradians. However, the opening angle of the BGO collimator corresponds to just 0.6 steradians, so about 90% of the surface gamma-ray flux passes through the shield before being detected by the NaI. On the surface of Eros, the NaI "sees" the asteroid mostly through the BGO shield, thus reducing the total efficiency. The BGO efficiency on the surface was calculated in a similar manner.

Theoretical Gamma-Ray-Flux Calculations

To convert the measured gamma-ray-flux ratios to abundance ratios, a series of calculations were done. These gamma-ray-production calculations were done in the same way that gamma-ray fluxes were calculated for Mars (Masarik and Reedy, 1996) and Mercury (Brückner and Masarik, 1997). The first calculations used the LAHET Code System (LCS) to numerically simulate the interactions of galactic-cosmic-ray (GCR) particles with the surfaces of asteroids of various compositions and the subsequent production and transport of the neutrons and protons that make gamma rays. The flux of GCR particles averaged over a solar cycle was used. These particle fluxes then were used to calculate the rates for producing gamma rays as a function of depth. The cross sections for nuclear reactions producing gamma rays by inelastic-scattering reactions and intensities of gamma rays made by neutron-capture reactions were those used earlier for the Moon and Mars (Reedy, 1978). The gamma rays made in the asteroid's surface by

these particles were then transported to the asteroid's surface. Only the fluxes of gamma-ray lines that escaped the surface without undergoing an interaction were considered.

Calculations of gamma-ray productions were done for a variety of meteorite compositions, including compositions of individual meteorites that were chosen to span the range of compositions expected, particularly for iron. These compositions were taken from the meteorite database (Nittler et al., 2001a). An assumed density of the meteorites (about 3 g/cm³) was used, although several calculations done with a density of 1 g/cm³, which is about that expected for the surface of an asteroidal regolith, gave the same results. The averaged lunar composition of Reedy (1978) was also used for comparisons with previous gamma-ray-flux calculations (Reedy, 1978; Masarik and Reedy, 1996).

The surface was assumed to be of uniform composition both vertically and horizontally. The meteorite compositions used in the calculations assumed no H or C, which can rapidly thermalize energetic neutrons and significantly increase the fluxes of gamma rays made by neutron-capture reactions (Masarik and Reedy, 1996). The assumed compositions also excluded such neutron-absorbing elements as Cl, Sm, and Gd that can reduce the fluxes of neutron-capture gamma rays from other elements (Reedy, 1978). In some cases (e.g., C in ureilites), these abundances were included in the data of Nittler et al. (2001a) and intentionally excluded from the calculations. In other case (e.g., Sm, Gd), abundances were not known. The major neutron-capture gamma rays expected from Eros are the 7.646 and 7.631 MeV gamma rays from Fe and the 4.934 and 3.539 MeV gamma rays from Si.

The fluxes of gamma rays made by inelastic-scattering reactions, such as those at 0.847 MeV from Fe, 1.779 and 6.878 MeV from Si, 1.369 and 2.754 MeV from Mg, and 6.129, 6.917, and 7.117 MeV from oxygen are only weakly affected by the bulk composition. High concentrations of elements with larger atomic masses, such as Fe, result in higher fluxes of the fast neutrons that make such inelastic-scattering gamma rays (Gasnault et al., 2001). The flux of the 1.461 MeV gamma ray made by the decay of naturally radioactive ⁴⁰K was also calculated.

The agreement with previous calculations done using LCS is good, and these calculations are consistent with earlier work. As noted in Masarik and Reedy (1996), gamma-ray-flux calculations done with LCS differ slightly from those done using other models for GCR interactions, such as those of Reedy (1978).

As the flux of GCR particles at Eros was low and not well known during the NEAR-Shoemaker mission, ratios of gamma-ray fluxes to ratios of elemental abundances were calculated for the cosmogenic gamma rays. For two gamma rays that are both made by the same type of nuclear reactions (inelastic scattering or neutron capture), e.g., the ratio of the fluxes of the 0.847 and 1.779 MeV inelastic-scattering gamma rays to the Fe/Si abundance ratio, such trend lines are very linear. There is some scatter about the trend line for the ratio of the 7.631 MeV Fe capture gamma rays to the 6.129 MeV oxygen inelastic-scattering gamma ray as a function of the iron to oxygen abundances in the meteorite models. The compositions that were the farthest from the trend line were those for the Moon that had significant amounts of the neutron-absorbing elements Ti, Sm, and Gd. In those cases, the flux ratios were lower than the trend line.

Fig. 11 shows two examples of results from these calculations. The upper plot shows the relationship between the ratio of the Fe capture line at 7.631 MeV to the oxygen inelastic line at 6.129 MeV compared to the ratio of iron to silicon in the meteorite models and a fit to the data. This ratio is particularly important as it can be determined independently from each of the four spectra. The lower curve shows the relationship between the ratio of the Fe inelastic line at 0.847 MeV to the Si inelastic line at 1.779 MeV and the ratio of iron to silicon in the meteorite models and a fit to the data. Calculations for one lunar (Reedy, 1978) and two Mercury compositions (Brückner and Masarik, 1997) are included for comparison. These curves are then used to convert the measured photon ratios to composition ratios.

RESULTS

The results for the elemental ratios determined from the gamma-ray measurements are given in **Table 1**. The results for the iron to oxygen ratio using the Fe 7.631 MeV capture line and the O 6.129 MeV inelastic line as derived for the four spectra are shown. The results for the silicon to oxygen ratio using the Si 4.934 MeV capture line and the O 6.129 MeV inelastic line are shown for three spectra. The other composition results are derived from the analysis of the anticoincidence spectrum. These include the iron to silicon ratio from both inelastic lines, the magnesium to silicon ratio from the inelastic lines, and the potassium concentration from the ^{40}K line. In addition the iron inelastic to iron capture photon ratio and the silicon inelastic to silicon capture photon ratio can be derived. These do not contain any useful geochemical results, but are an indication of the hydrogen content of the sample. The gamma-ray calculations all assume zero hydrogen content and derive the iron and silicon inelastic to capture photon ratios on that basis. Comparison with measurements should indicate the validity of that assumption. Smaller values of the inelastic to capture ratios would indicate the presence of hydrogen, even if it could not be detected by the neutron capture line from hydrogen. Typical calculated values for the ratio of the iron inelastic line (at 0.847 MeV) to the iron capture line (at 7.631 MeV) for many meteorites are around 1.8, though values can range to over 3 compared to a derived value of 2.9. Typical calculated values for the ratio of the silicon inelastic line (at 1.779 MeV) to the silicon capture line (at 3.539 MeV) for many meteorites are about 10.5, though values can range up to 13 compared to a derived value of 11.9. The high values for these ratios are typically for iron-nickel rich meteorites (e.g., mesosiderites). Because these ratios are derived from a low energy gamma ray and a high energy gamma ray, these ratios are dependent on the accuracy of the calculated efficiencies. Considering these uncertainties, the two derived values for the inelastic to capture ratios are both in reasonable agreement with the calculated values and indicate the assumption of zero hydrogen is valid.

Realistic uncertainties for these derived compositions are difficult to estimate. The statistical uncertainties can be derived from the measurements and the background subtraction. These statistical uncertainties tend to be small, typically between 5 and 10 percent. Another source of uncertainty is due to the response functions that may not be linearly independent and the spectral shapes can interfere with on another in fitting the data (Reedy et al., 1973). Another uncertainty is in the calculation of the detector efficiency. While efficiencies for gamma ray ratios close in energy are probably valid, those far apart in energy have an additional uncertainty associated with the result. Perhaps the best measure of the uncertainty in determining the elemental ratios is the spread in the result for the same ratio. For the iron to oxygen ratio there are four values

calculated independently ranging from 0.16 to 0.44 with a mean value of 0.28 and a standard deviation of 0.12 (40 %). The other result that has multiple values is the silicon to oxygen ratio with a mean value of 0.61 and a standard deviation of 0.05 (8%), but without a value from the BGO spectrum. Because of the energy resolution, the BGO spectrum is more difficult to analyze and only the results for the highest energy lines were determined. As a conservative approach, we assume that this 40% uncertainty applies for all the GRS results.

DISCUSSION

Two of the major goals of the NEAR mission are to relate 433 Eros to known groups of meteorites and to decipher the geologic history of Eros through both analysis of returned data and comparison with meteorites. Before trying to address these questions, it is fair to ask whether Eros can or should be compared to meteorites. While we know that most meteorites originate from asteroids, there is no *a priori* reason to assume that we have a sample of Eros in our collections. Eros is not currently in a location dynamically favorable for delivery of meteorites to Earth (Zappala et al., 1998; Michel et al., 1999). However, we also know that near-Earth asteroids are dynamically unstable over the lifetime of the Solar System and are almost certainly replenished from the main belt. In the case of Eros, removal from the main belt into the near-Earth population may have occurred within the last 100 million years (e.g., Bottke et al., 2000), possibly with a source from the Maria family of asteroids (Zappala et al., 1997). Thus, Eros probably originated in a location favorable for delivery of meteorites to Earth and, although we may not have a piece of Eros in our collections, we probably have similar material.

In comparing the chemical composition of Eros to that of asteroids, the first question we might ask is whether Eros has the same composition as an ordinary chondrite, given the abundance of both S-type asteroids and ordinary chondrites. Almost all meteorites have Si/O ratios in the range of 0.35-0.6 so while the GRS results are within this range this ratio cannot give us much information concerning meteorite comparisons. **Fig. 12** plots the Mg/Si vs. K for a wide array of meteorite types, as well as the GRS-derived value for 433 Eros (with the 40% uncertainty ellipse). We find that the composition of Eros overlaps that of H, L and LL ordinary chondrites, although the error ellipse would also allow other types of chondrites (carbonaceous, enstatite, R) and primitive achondrites (acapulcoites, brachinites, winonaites). Most meteorites from fully-differentiated bodies (e.g., howardites, eucrites, diogenites, aubrites) are excluded.

The finding of a chondritic composition from the GRS-derived Mg/Si and K values is in close agreement with compositions derived from the XRS, MSI and NIS experiments, all of which point to a chondritic composition. Indeed, the Mg/Si ratio derived by XRS and GRS are similar. It is interesting to note that K is apparently not depleted in the GRS composition. The marked S/Si depletion noted by XRS has been explained by surface depletion of this volatile element during micrometeorite bombardment and sputtering (Trombka et al., 2000). It was thought that the volatile element K might show a similar depletion, though this would not necessarily appear in the GRS results.

While the match between XRS- and GRS-derived Mg/Si ratios is noteworthy, the picture becomes somewhat more complicated if we consider Fe/Si and Fe/O ratios. **Fig. 13** plots Mg/Si vs. Fe/Si for the X-ray and gamma ray derived values for 433 Eros. While the XRS value is

similar to H chondrites (as well as some carbonaceous chondrites and primitive achondrites), the GRS ratios include LL and L chondrites, some primitive achondrites, angrites, diogenites and howardites. Note that there is no overlap of the statistical uncertainties between the XRS and GRS derived values.

The mismatch becomes even more apparent if we examine a plot of Fe/Si vs. Fe/O in **Fig. 14**. On this plot, virtually all meteorites define a straight line. The only notable exceptions are hydrated carbonaceous chondrites. The gamma-ray derived values of 433 Eros plot, on average, slightly above the line with an error ellipse that includes howardites, eucrites, diogenites, ureilites and angrites, but not ordinary chondrites.

There are three possible interpretations for the apparent mismatch between the XRS and GRS derived values. First, the mismatch might result from errors in the calculation of elemental compositions from raw spectra of either the XRS or GRS experiment. The gamma-ray lines used for Fe, Si and O are all at relatively high energies and any uncertainties associated with the calculated detector efficiencies tend to cancel out when taking ratios. In addition, the iron and oxygen lines should be among the strongest lines in the spectra and, thus, should have the greatest degree of confidence in the results of the spectral analysis. Thus, we think it unlikely that the mismatch results from incorrect analysis of the GRS spectra.

If we recall that the XRS and GRS measurements sample at both different depths (tens of cms for GRS vs. tens of microns from XRS) and spatial scale (submeter for *in situ* GRS vs. several kms for orbital XRS), the other two interpretations become apparent. The second explanation is that 433 Eros really is partially differentiated, with the scale of melting being somewhere between the meter scale of the GRS and the few km scale of the XRS. We find this scenario improbable, although we cannot dismiss it completely. Our skepticism arises both from our understanding of the geologic processes that create the differentiated meteorites and the required scale of differentiation. Howardites, eucrites and diogenites are thought to be products of near-total melting at a global scale. On 433 Eros, we can be confident that global melting did not occur, owing to the chondritic Al/Si and Ca/Si ratios derived by the X-ray experiment (Nittler et al., 2001b). It is unclear whether melting on a smaller scale could actually produce these lithologies. More importantly, extensive differentiation, even on a small spatial scale, should produce dramatically different lithologies, including basaltic, dunitic and metallic. Yet, the multi-spectral imager experiment, which has spatial resolution on the order of tens of meters, did not detect the type of lithologic heterogeneity inferred by this model. Thus, we consider such a scenario highly unlikely.

The third, and much more probable, scenario is that processes occurring within the regolith of 433 Eros produced the anomalously low Fe/O and Fe/Si ratios. Veverka et al. (2001b) have made compelling arguments that the regolith on the surface of Eros may be up to several meters thick in some areas. This regolith is the end product of a history of bombardment that might extend back millions to billions of years. The landing site of the NEAR-Shoemaker spacecraft was particularly smooth and may have been at the end of a “pond” deposit – flat material that infilled existing lows and could have formed by a variety of mechanisms. It is worth considering whether this material might differ from known meteorites and whether physical processes occurring within the regolith might explain the discrepancy.

In answer to the first question, meteorites are undoubtedly a poor sample of modern asteroid regolith (McKay et al., 1989). Even meteoritic regolith breccias, which contain solar wind gases and must have been exposed at the surface of the asteroid, may only contain a small fraction of the optical regolith and may have been indurated billions of years ago. Thus, there is no reason to assume that we have adequately sampled the regolith of any asteroid, let alone 433 Eros.

The second question is more difficult to answer. To explain the lower Fe/Si and Fe/O ratios of the in situ GRS measurement relative to a chondritic bedrock, a marked depletion of iron must occur. Such a depletion points to separation of the metal and sulfide (FeS) from the silicates. Several mechanisms exist to produce such a separation. Robinson et al. (2001) have argued that electrostatic migration may play a key role in infilling ponds. Such a mechanism may operate differently on conductive metal compared to non-conductive silicates. Metal and silicates would differ dramatically in density (8 vs. 3 g/cc) and, possibly, size (due to differences in brittle/ductile behavior) within the regolith of an asteroid. This could lead to preferential migration of metal relative to silicate. It is unclear whether metal would rise (e.g., the Brazil nut effect) or sink as a result of these differences, but either might explain a surficial enrichment or depletion of metal. We have also considered whether the low Fe/O and Fe/Si ratios derived by GRS can be explained by depletion of metal from a chondritic bedrock. The silicate portion of an H chondrite would have a Fe/Si ratio of 0.4 and a Fe/O ratio of 0.2. These results suggest that incomplete removal of metal and sulfide from an H chondrite could explain the composition of 433 Eros. Such removal would have no effect on the Mg/Si ratio or K abundance. Interestingly, the same is true for LL chondrites, which have less metal to remove, but lower Fe/Si and Fe/O ratios in bulk. These results suggest that metal (\pm sulfide) migration in the regolith of 433 Eros might explain the discrepancy between the XRS and GRS results. As noted by Nittler et al. (2001b), they also suggest that it may not be possible to point to a single, unambiguous meteoritic analog for 433 Eros. An attempt to define such an analog combining the XGRS and MSI/NIS results is presented by McCoy et al. (2001).

ACKNOWLEDGMENTS

We thank the NEAR project at APL, particularly the management teams led by T. B. Coughlin, R. W. Farquhar, R. E. Gold, and M. E. Holdridge and the JPL navigation team led by B. G. Williams who managed to set the spacecraft on Eros so expertly that the GRS was able to collect data on the surface for more than two weeks. We thank the personnel at the DSN for their expertise in bringing back the data from Eros. We also thank the XGRS data management teams lead by Tim McClanahan at Goddard and Jessie Bhangoo at the University of Arizona for their continuing support. This work was supported by NASA. The work at Los Alamos was done under the auspices of the US Department of Energy. We thank the reviewers, David J. Lindstrom and Gregory W. Kallemeyn, for their helpful comments and suggestions.

REFERENCES

- BIELEFELD M. J., REEDY R. C., METZGER A. E., TROMBKA J. I., and ARNOLD, J. R. (1976) Surface chemistry of selected lunar regions. *Proc. Lunar Planet. Sci.* **7th**, 2661-2676.
- BOTTKE W. F. Jr., JEDICKE R., MORBIDELLI A., PETIT J. M., and GLADMAN B. (2000) Understanding the distribution of near-Earth asteroids. *Science* **288**, 2190-2194.
- BOYNTON W. V., ET AL. (1992) Science applications of the Mars Observer gamma ray spectrometer. *J. Geophys. Res.* **97**, 7681-7698.
- BOYNTON W. V., EVANS L. G., REEDY R. C., and TROMBKA J. I., (1993) The Composition of Mars and Comets by Remote and In-Situ Gamma-Ray Spectrometry, in *Remote Geochemical Analysis: Geochemical and Mineralogical Composition*, ed. C. PIETERS and P. ENGLERT, Cambridge University Press, New York, 395-412.
- BRÜCKNER J., ET. AL. (1991) Proton-induced radiation damage in germanium detectors. *IEEE Trans. Nucl. Sci.*, **NS-38**, 209-217.
- BRÜCKNER J. and MASARIK J., (1997) Planetary gamma-ray spectroscopy of the surface of Mercury. *Planet. Space Sci.* **45**, 39-48.
- DYER C. S., TRUSCOTT P., EVANS L. and TROMBKA J. (1998) Comparison between predictions & observations of induced radioactive background in interplanetary missions. In *Conference on the High Energy Radiation Background in Space*, pp. 53-57. IEEE, Piscataway, NJ.
- EVANS L. G., REEDY R. C., and TROMBKA J. I., (1993) Introduction to planetary remote sensing gamma ray spectroscopy in *Remote Geochemical Analysis: Elemental and Mineralogical Composition*, C. PIETERS and P. ENGLERT (ed), Cambridge University Press, Cambridge, New York, 167-198.
- EVANS L. G., CLARK P. E., and TROMBKA J. I., (1995) A small X-ray/gamma-ray geochemical experiment package for discovery class missions. *Acta Astron Suppl.*, **35**, 79-88.
- EVANS L. G., STARR R. D., TROMBKA J. I., MCCLANAHAN T. P., BAILEY S. H., MIKHEEVA I., BHANGOO J., BRÜCKNER J., and GOLDSTEN J. O. (2000) Calibration of the NEAR gamma-ray spectrometer. *Icarus*, 148,95-117.
- GASNAULT O., FELDMAN W. C., MAURICE S., GENETAY I. and D'USTON C. (2001) The first lunar map of the average soil atomic mass (abstract). *Lunar Planet. Sci.* **32**, #1963. Lunar and Planetary Institute, Houston, Texas, USA (CD-ROM).
- GAFFEY M. J., BURBINE T. H., PIATEK J. L., REED K. L., CHAKY D. A., BELL J. F. and BROWN R. H. (1993) *Icarus* **106**, 573-602.

- GOLDSTEN J. O., ET. AL. (1997) The x-ray/gamma-ray spectrometer on the Near Earth Asteroid Rendezvous Mission. *Sp. Sciences Rev.*, **82**, 169-216, (1997).
- KNOLL G. F., (1989) *Radiation Detection and Measurement*. Wiley, New York.
- MASARIK J. and REEDY R. C. (1996) Gamma ray production and transport in Mars. *J. Geophys. Res.* **101**, 18,891-18,912.
- MCCOY T. J., ET. AL. (2001) The composition of 433 Eros: a mineralogical-chemical synthesis, submitted to *Meteorit. Planet. Sci.*
- MCKAY D. S., SWINDLE T. D., and GREENBERG R. (1989) Asteroidal regolith: What we do not know in *Asteroids II* (R. P. BINZEL, T. GEHRELS, and M. S. MATHEWS, eds.) U. of Arizona Press, Tucson, AZ, pp. 617-642.
- MICHEL P., GONCZI R., FARINELL A P. and FROESCHLE C. H., (1999) Dynamical evolution of 1036 Ganymed, the largest near-Earth asteroid. *Astron. Astrophys.* **347**, 711-719.
- NITTLER L. R., MCCOY T. J., CLARK P. E., MURPHY M. E., TROMBKA J. I., and JAROSEWICH E. (2001a) Bulk element compositions of meteorites: Linking asteroids and meteorites and understanding their formation, submitted to *Meteorit. Planet. Sci.*
- NITTLER L. R., ET. AL. (2001b) X-ray fluorescence measurements of the surface elemental composition of asteroid 433 Eros, submitted to *Meteorit. Planet. Sci.*
- REEDY R. C., ARNOLD J. R., and TROMBKA J. I., (1973) Expected γ ray emission spectra from the lunar surface as a function of chemical composition. *J. Geophys. Res.* **78**, 5847-5866.
- REEDY R. C., (1978) Planetary gamma-ray spectroscopy. *Proc. Lunar Planet. Sci.* **9th**, 2961-2984.
- ROBINSON M. S., THOMAS P. C., VEVERKA J., MURCHIE S., AND CARCICH B. (2001) The nature of ponded deposits on Eros. *Nature*, **413**, 396-400.
- TROMBKA J. I., ET. AL. (1979) Analytical Methods in Determining Elemental Composition from the Apollo X-Ray and Gamma-Ray Spectrometer Data, in *Computers in Activation Analysis and Gamma-ray Spectroscopy*, DOE Conf. 780421, 26.
- TROMBKA J. I., ET. AL. (1997) Compositional mapping with the NEAR x-ray/gamma-ray spectrometer. *J. Geophys. Res.* **102**, 23,729-23,750.
- TROMBKA J. I., ET. AL. (2000) The elemental composition of asteroid 433 Eros: results of the NEAR-Shoemaker X-ray spectrometer. *Science*, **289**, 2101-2105.
- TROMBKA, J. I., ET. AL. (2001) The NEAR-Shoemaker XGRS experiment: overview and lessons learned. Submitted to *Meteorit. Planet. Sci.*

VEVERKA J., ET. AL. (2001a) Imaging of small-scale features on 433 Eros from NEAR: evidence for a complex regolith. *Science*, **292**, 484-488.

VEVERKA J., ET. AL. (2001b) The landing of the NEAR-Shoemaker spacecraft on asteroid 433 Eros. *Nature*, **413**, 390-393.

WETHERILL G. W. (1985) Asteroidal source of ordinary chondrites. *Meteoritics*, **20**, 1-22.

ZAPPALA V., CELLINO A., DI MARTINO M., MIGLIORINI F., and PAOLICCHI P. (1997) Maria's family: Physical structure and possible implications for the origin of giant NEAs. *Icarus*, **129**, 1-20.

ZAPPALA V., CELLINO A., GLADMAN B. J., MANLEY S., and MIGLIORINI F. (1998) Asteroid showers on Earth after family breakup events. *Icarus* **134**, 170-176.

Table 1. GRS Composition Results.

Result	Anticoincidence	First Escape	Second Escape	BGO
Fe(7631)/O(6129)				
Photon ratio	0.79	0.43	0.42	0.32
Composition ratio	0.44	0.27	0.26	0.16
Si(4934)/O(6129)				
Photon ratio	0.24	0.28	0.30	
Composition ratio	0.53	0.63	0.67	
Fe(847)/Si(1779)				
Photon ratio	0.65			
Composition ratio	0.8			
Mg(1369)/Si(1779)				
Photon ratio	0.75			
Composition ratio	0.75			
K(1461)				
Photons/s	0.11			
Composition	0.07%			
Fe(847)/Fe(7631)				
Photon ratio	2.9			
Si(1779)/Si(3539)				
Photon ratio	11.9			

Note: Energies of gamma-ray lines in parenthesis are given in keV

FIGURE CAPTIONS

Figure 1. The three spectra were taken during July 2000 in the 35 km orbit. There was a large solar particle event on July 14, 2000. Shown are a spectrum taken on July 13 and two spectra taken on July 18 and 20 after the GRS was turned-on again.

Figure 2. An anticoincidence spectrum taken during December 2000 and January 2001 while in 35 km orbit and when the GRS was pointed at the asteroid is shown along with a spectrum taken while in the 200 km orbit and the difference between the two spectra is shown in the upper portion. The lower portion shows the difference on a linear scale.

Figure 3. A second escape spectrum taken during December 2000 and January 2001 while in 35 km orbit and when the GRS was pointed at the asteroid is shown along with a spectrum taken while in the 200 km orbit and the difference between the two spectra is shown in the upper portion. The lower portion shows the difference on a linear scale.

Figure 4. Five spectra are shown that were taken on the surface of Eros. The first escape and second escape spectra were divided by 2 and 4, respectively, for better visualization.

Figure 5. The calculated response function for $O(n,n'\gamma)$ is shown for the anticoincidence, first escape, and second escape spectra.

Figure 6. The lower energy portion of the surface anticoincidence spectrum is shown with the spline fit to the background and the difference spectrum is shown in the top portion. The lower portion shows the results of a least squares fit of the elemental response functions to the difference spectrum.

Figure 7. The higher energy portion of the surface anticoincidence spectrum is shown with the spline fit to the background and the difference spectrum is shown in the top figure. The lower figure shows the results of a least squares fit of the elemental response functions to the difference spectrum.

Figure 8. The surface first escape spectrum is shown with the spline fit to the background and the difference spectrum is shown in the top figure. The lower figure shows the results of a least squares fit of the elemental response functions to the difference spectrum.

Figure 9. The surface second escape spectrum is shown with the spline fit to the background and the difference spectrum is shown in the top figure. The lower figure shows the results of a least squares fit of the elemental response functions to the difference spectrum.

Figure 10. Calculated GRS efficiencies for the central detector used for measurements taken on the surface of Eros.

Figure 11. Two examples of calculated results of gamma-ray fluxes for different meteorite compositions. The upper figure shows the ratio of the iron 7631 keV capture line to the oxygen 6129 keV inelastic line versus the ratio of iron to oxygen composition. The lower curve shows the ratio of the iron 847 keV inelastic line to the silicon 1779 keV inelastic line versus the ratio of iron to silicon. Calculations for one lunar and two Mercury compositions are included for comparison.

Figure 12. The GRS result for the magnesium to silicon ratio is plotted against the potassium abundance with the assumed 40% uncertainty ellipse. Included are results from the meteorite database for these same two quantities.

Figure 13. The GRS result for the magnesium to silicon ratio is plotted against the iron to silicon ratio with the assumed 40% uncertainty (large ellipse). Included are results from the meteorite database for these same two ratios. Also shown are the XRS results and the uncertainty (small ellipse) associated with these results.

Figure 14. The GRS result for the iron to silicon ratio is plotted against the iron to oxygen ratio with the assumed 40% uncertainty ellipse. Included are results from the meteorite database for these same two ratios.

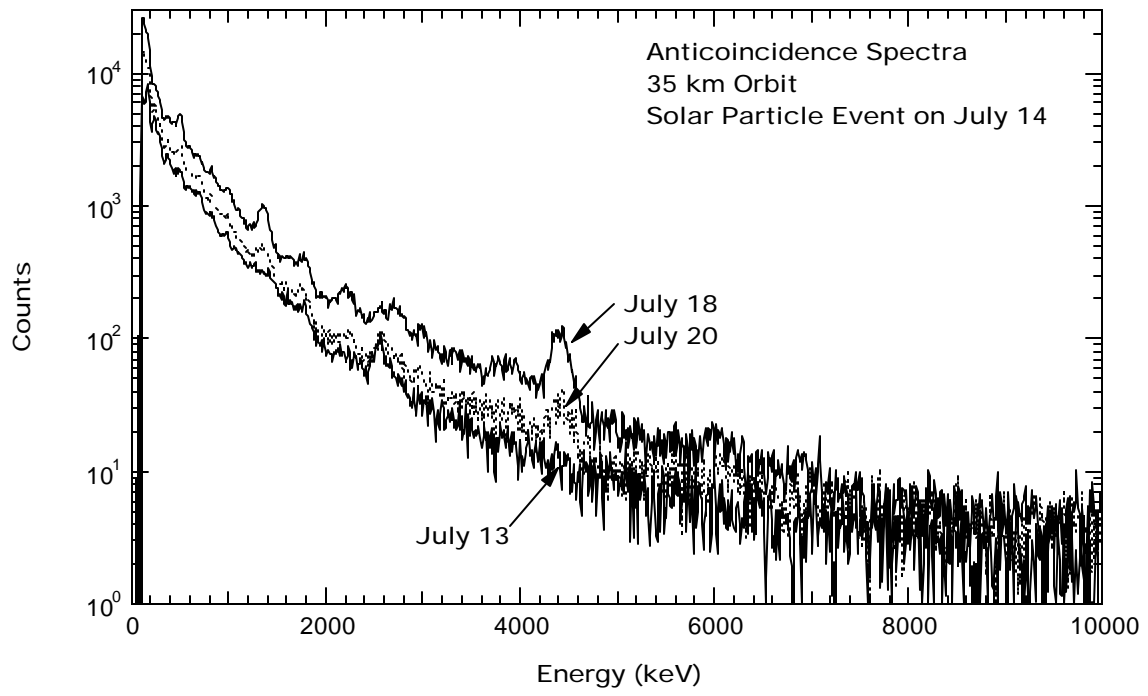


Figure 1.

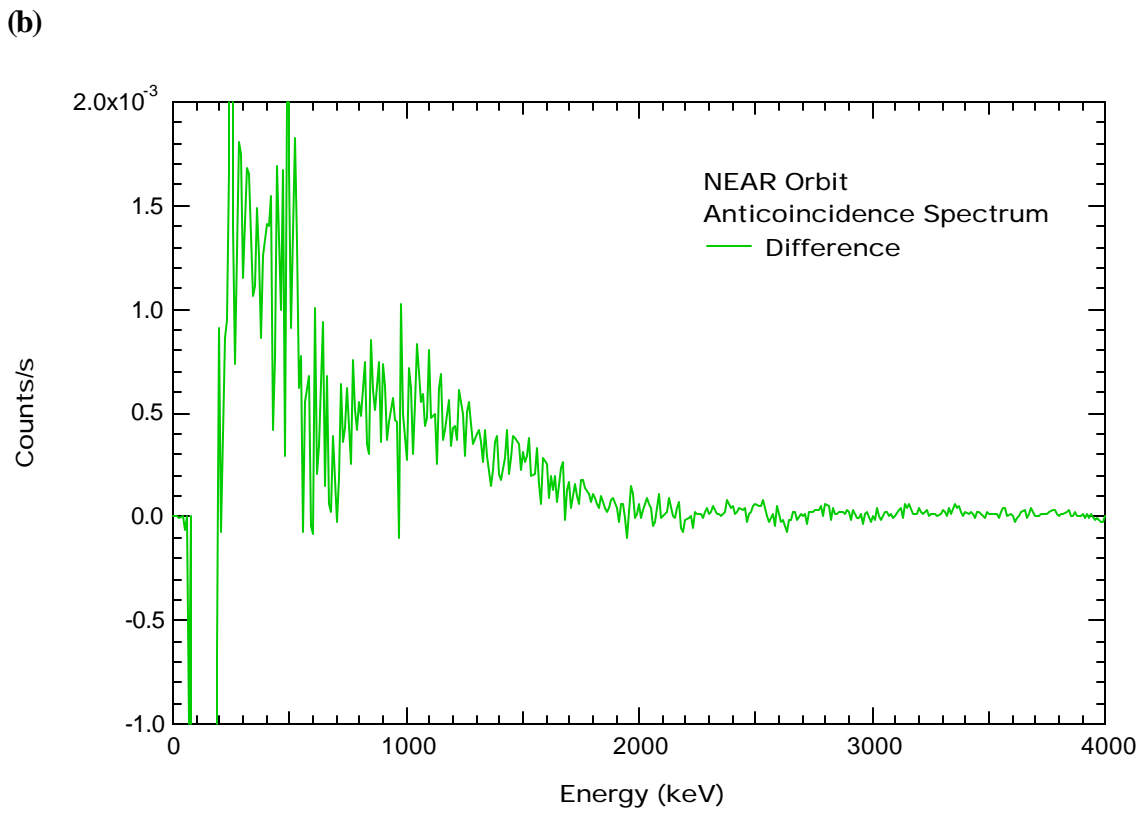
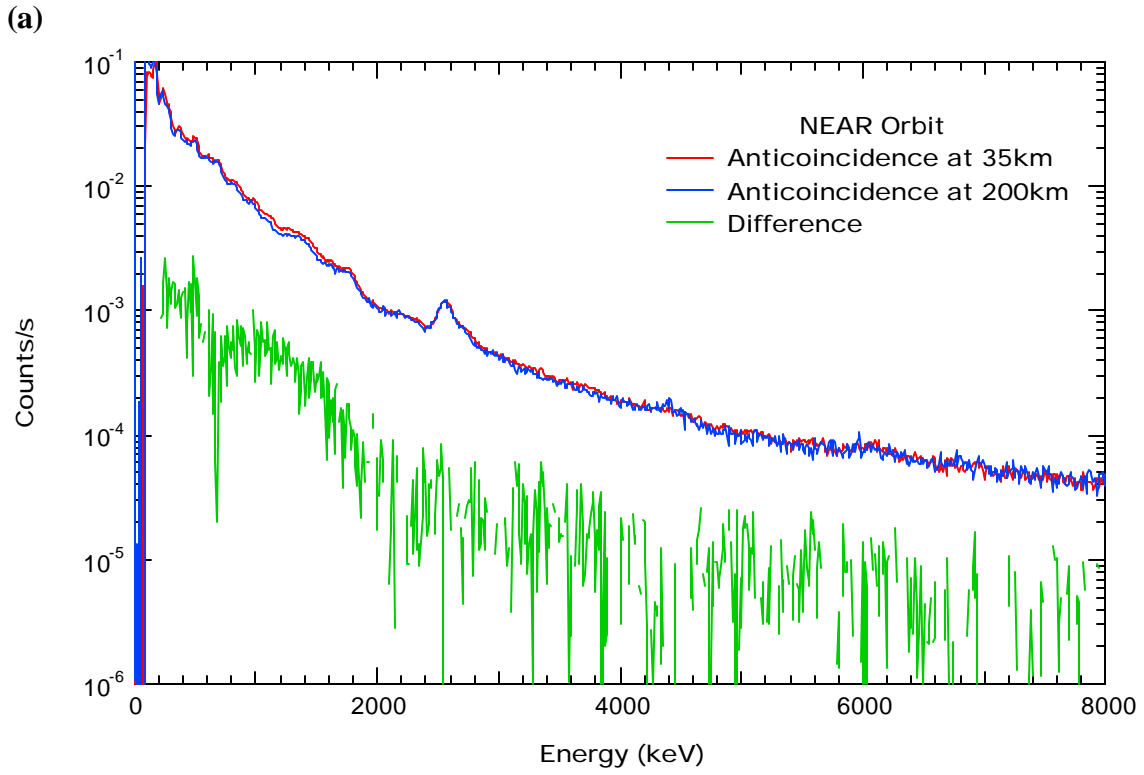


Figure 2.

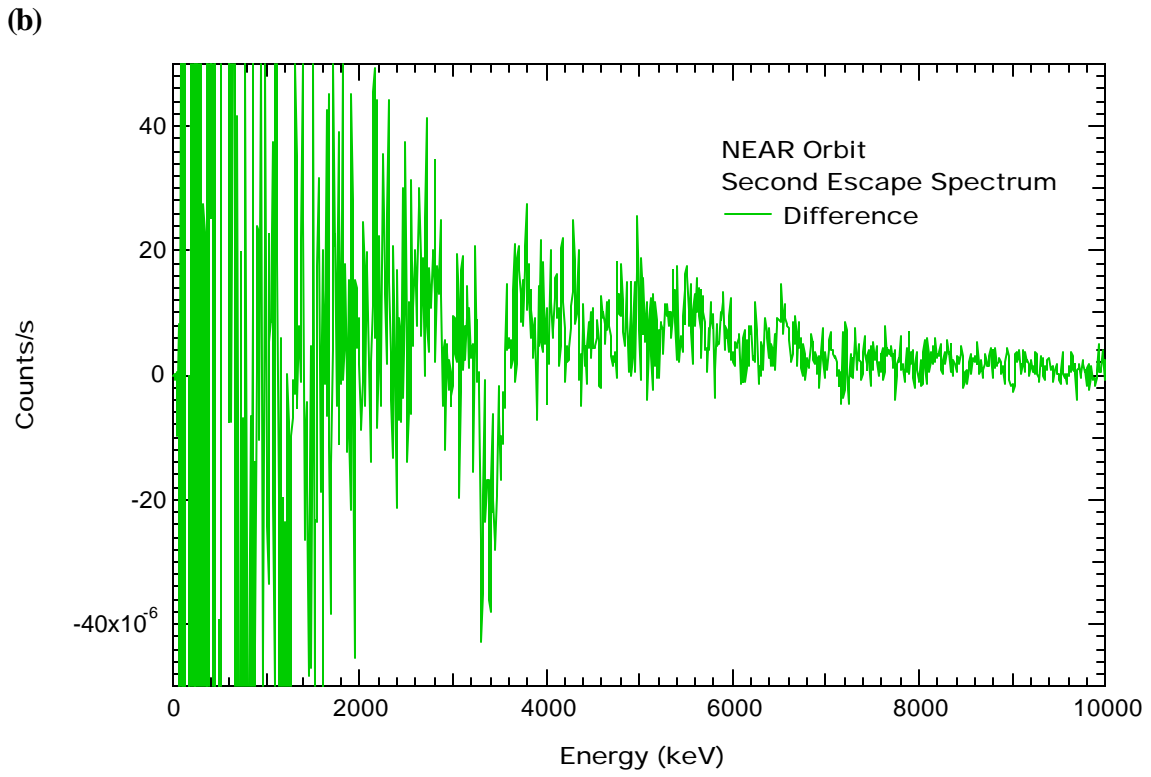
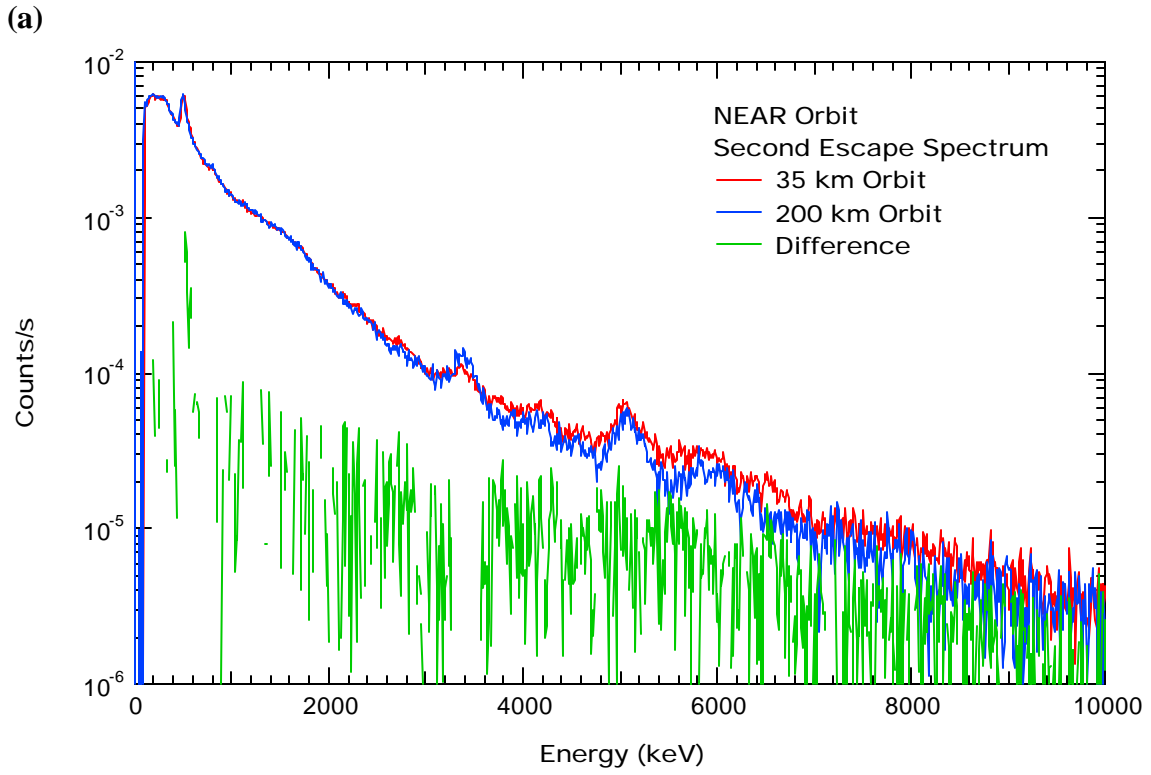


Figure 3.

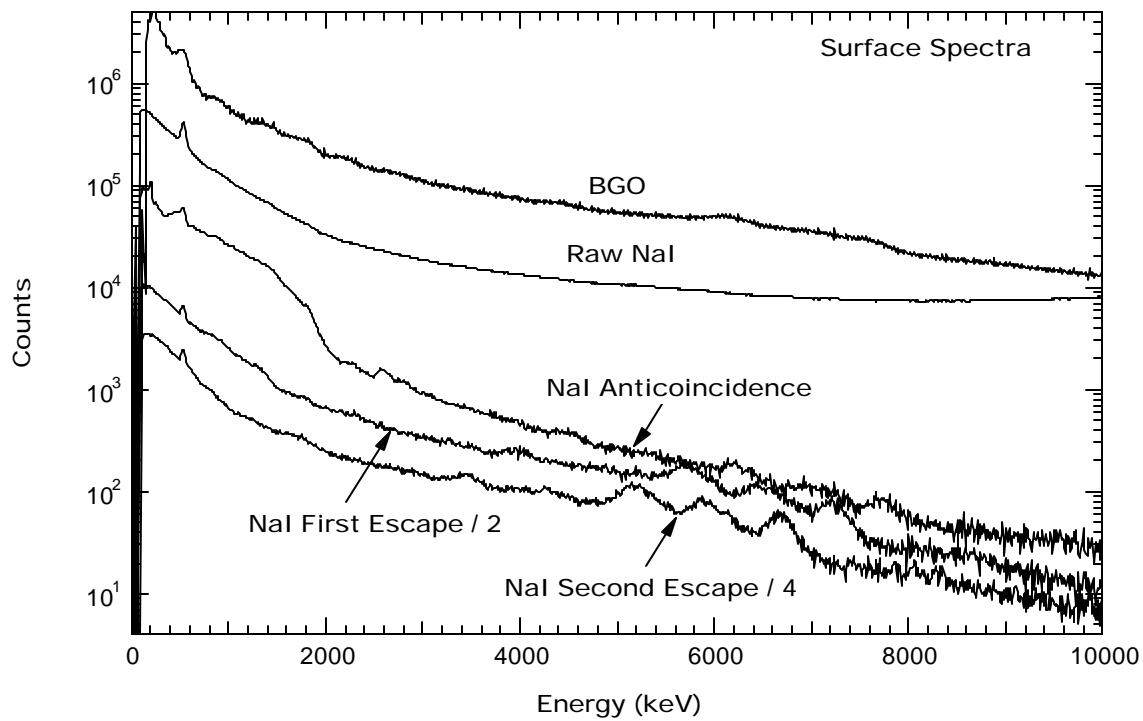


Figure 4.

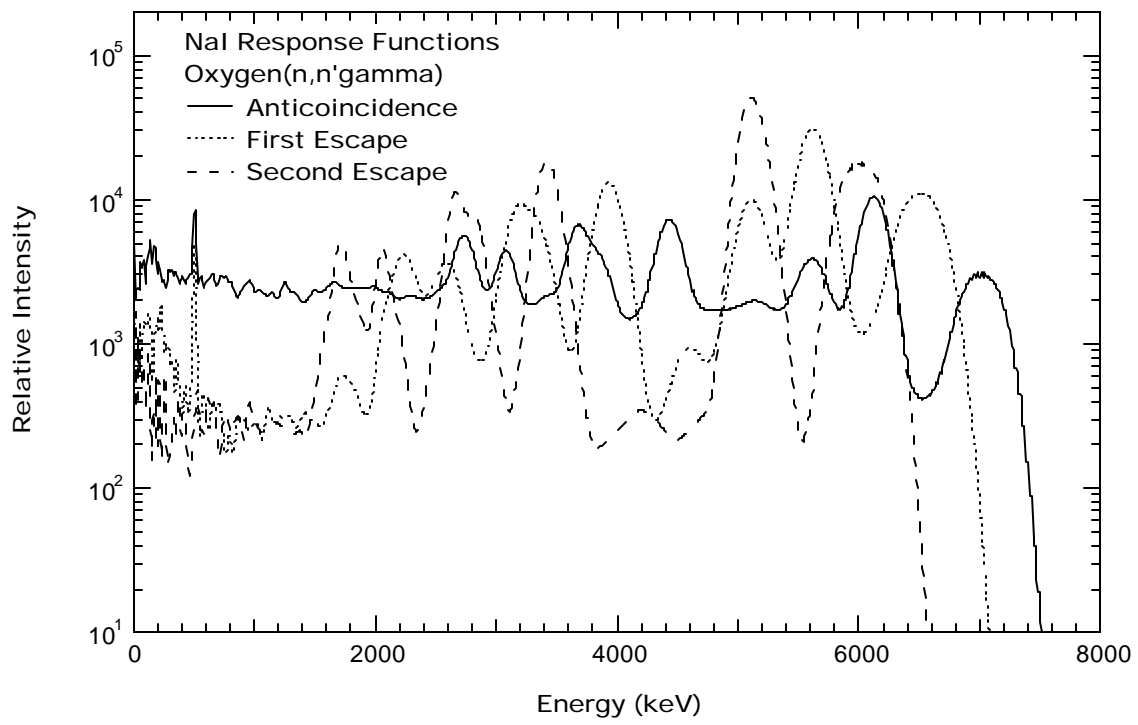
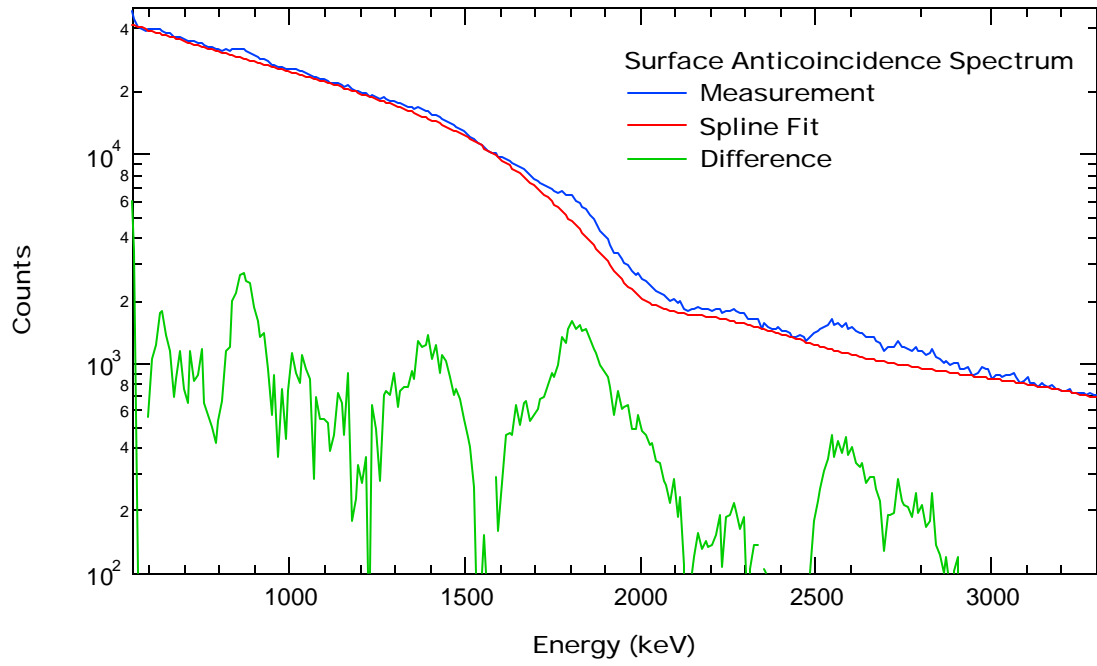


Figure 5.

(a)



(b)

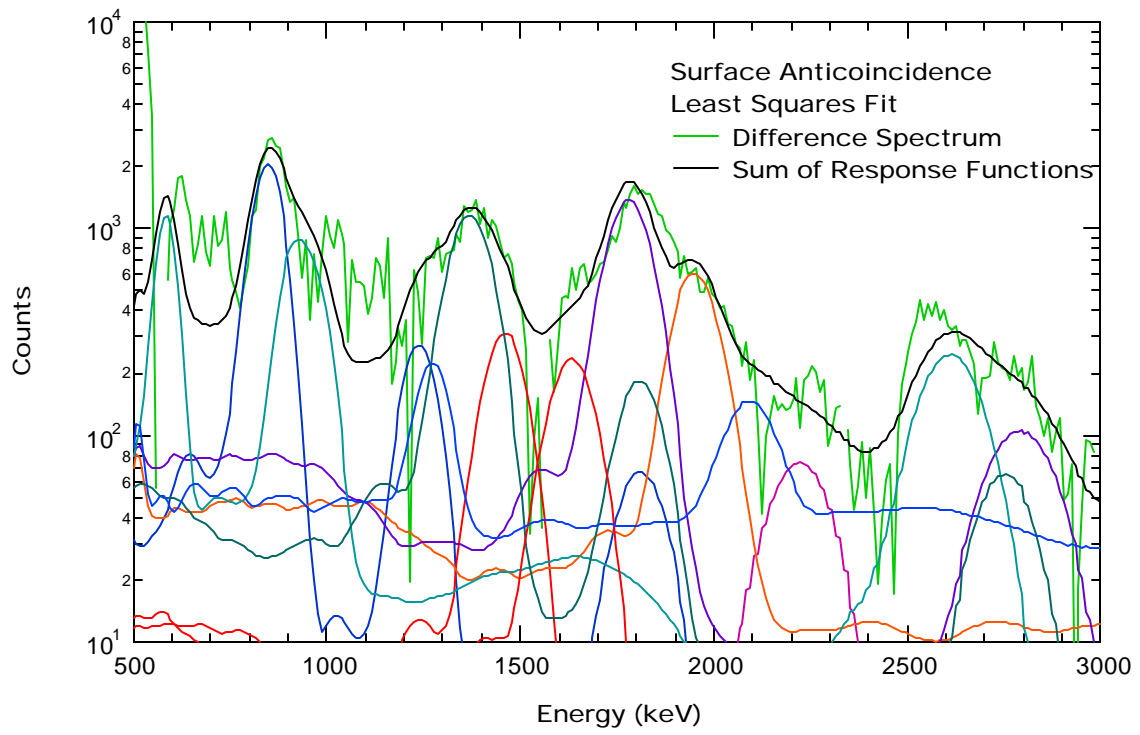


Figure 6.

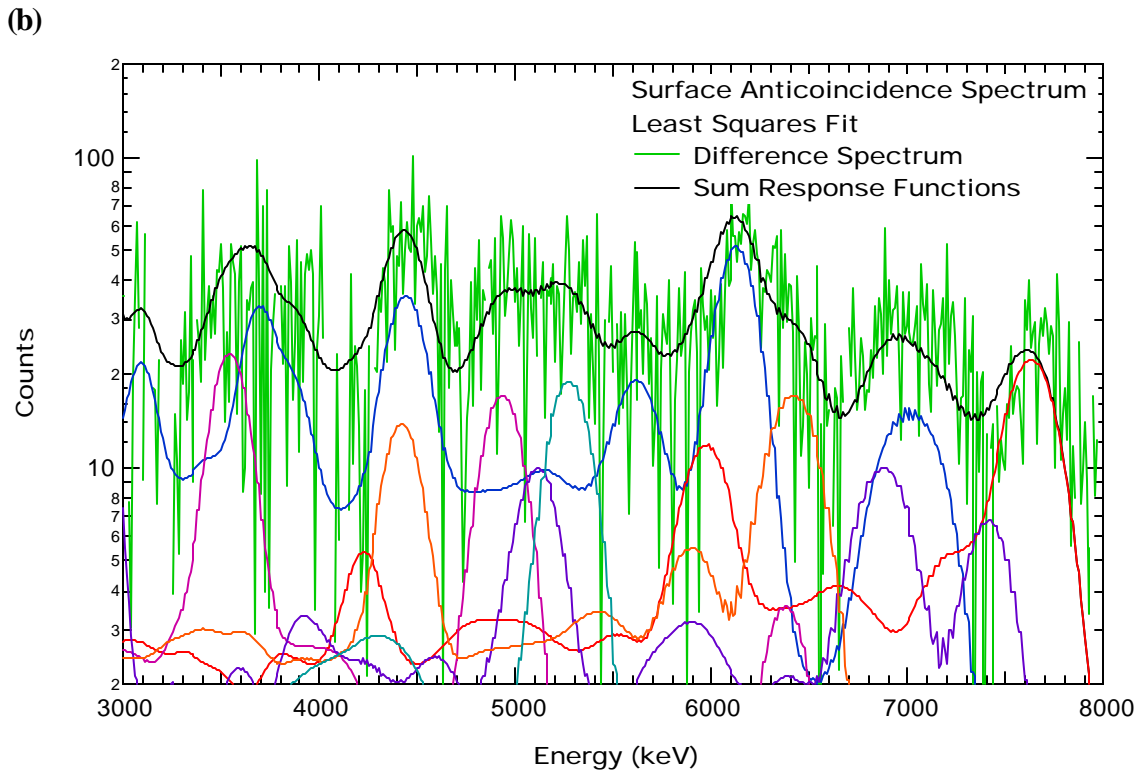
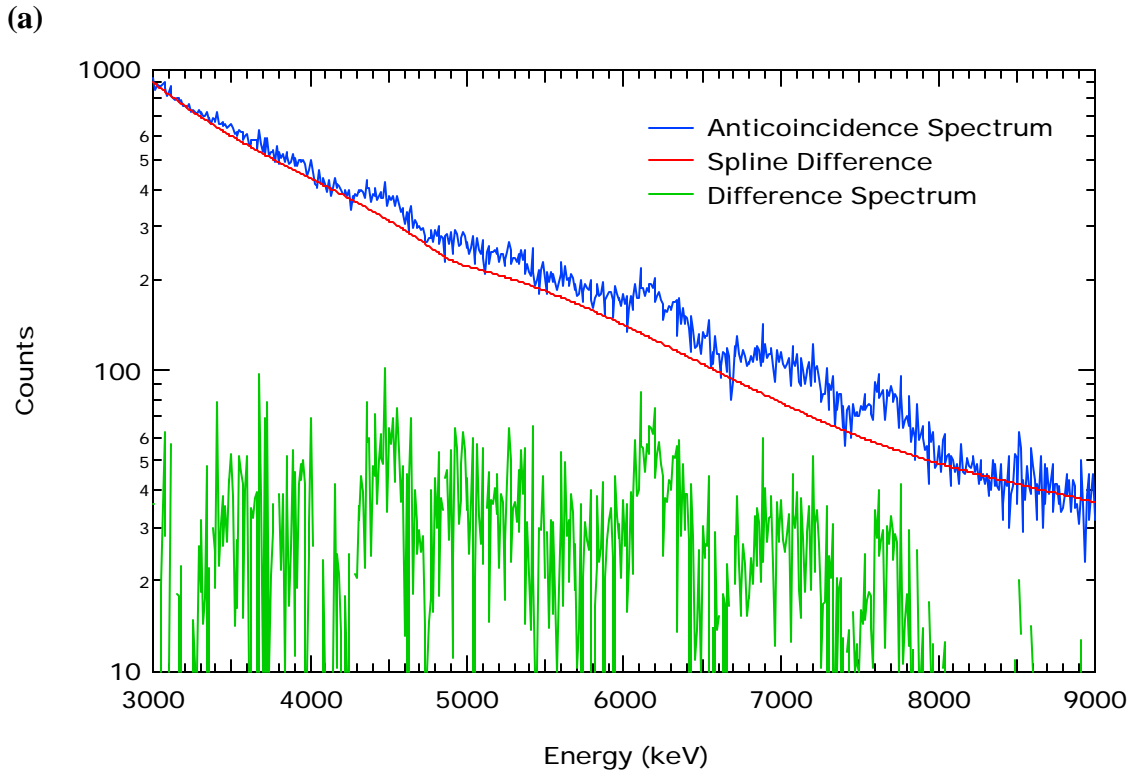


Figure 7.

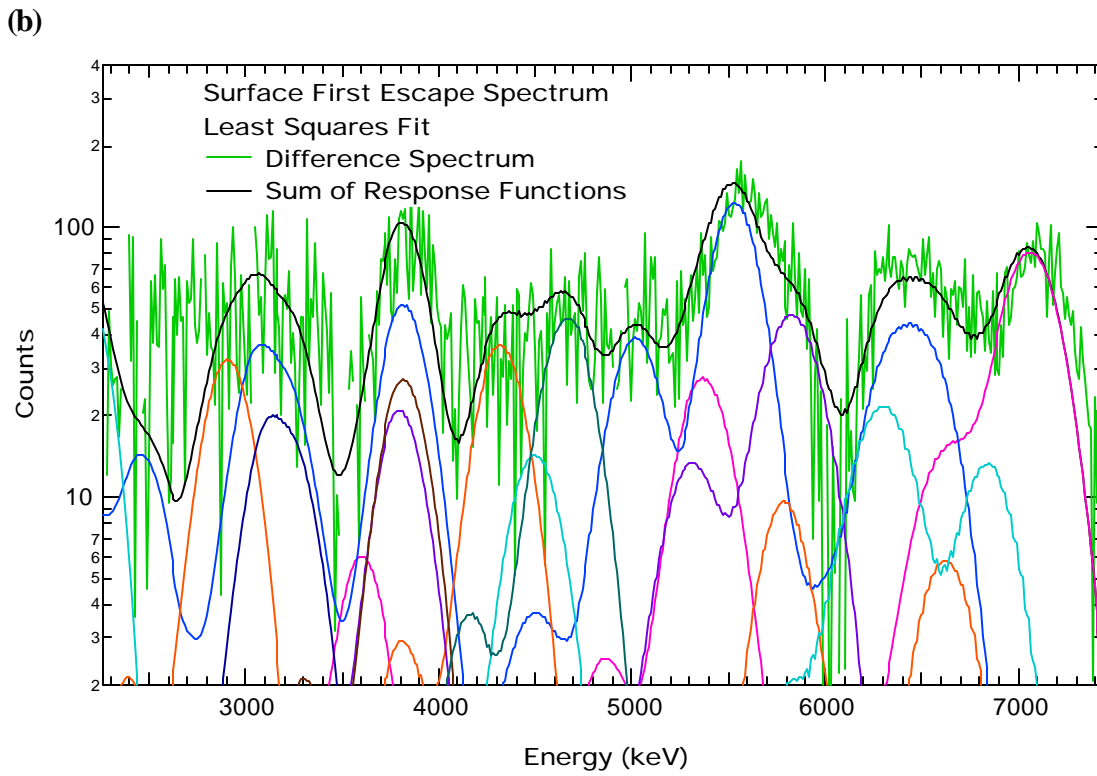
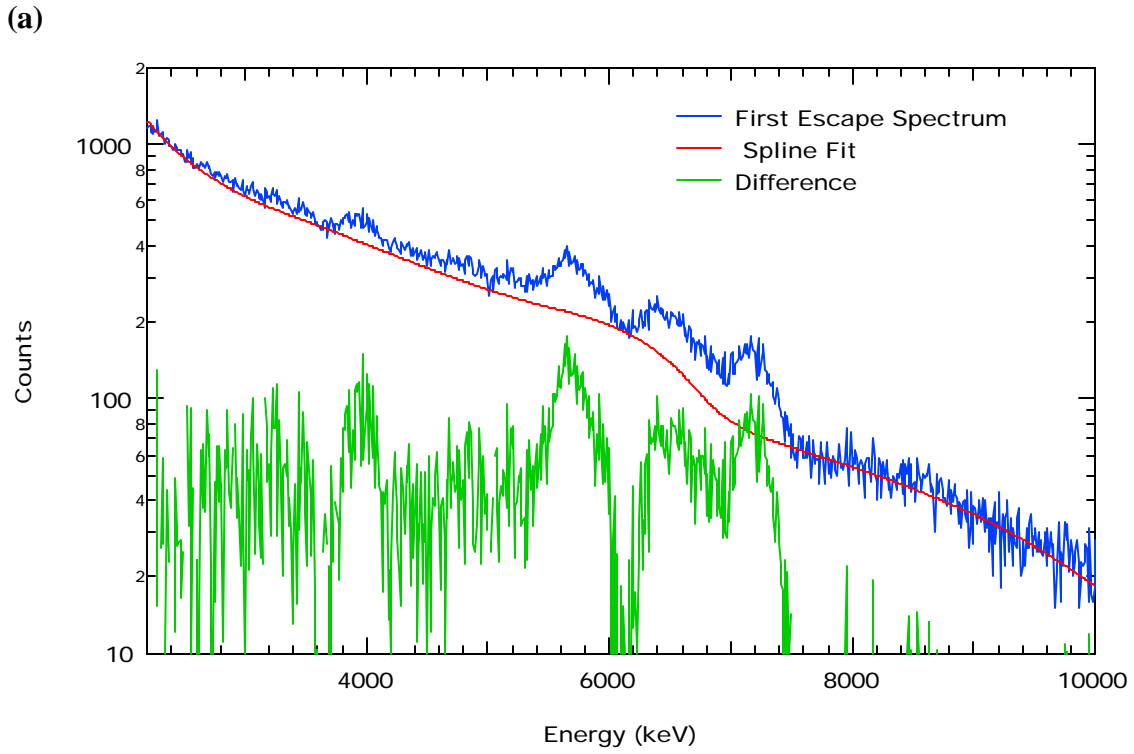


Figure 8.

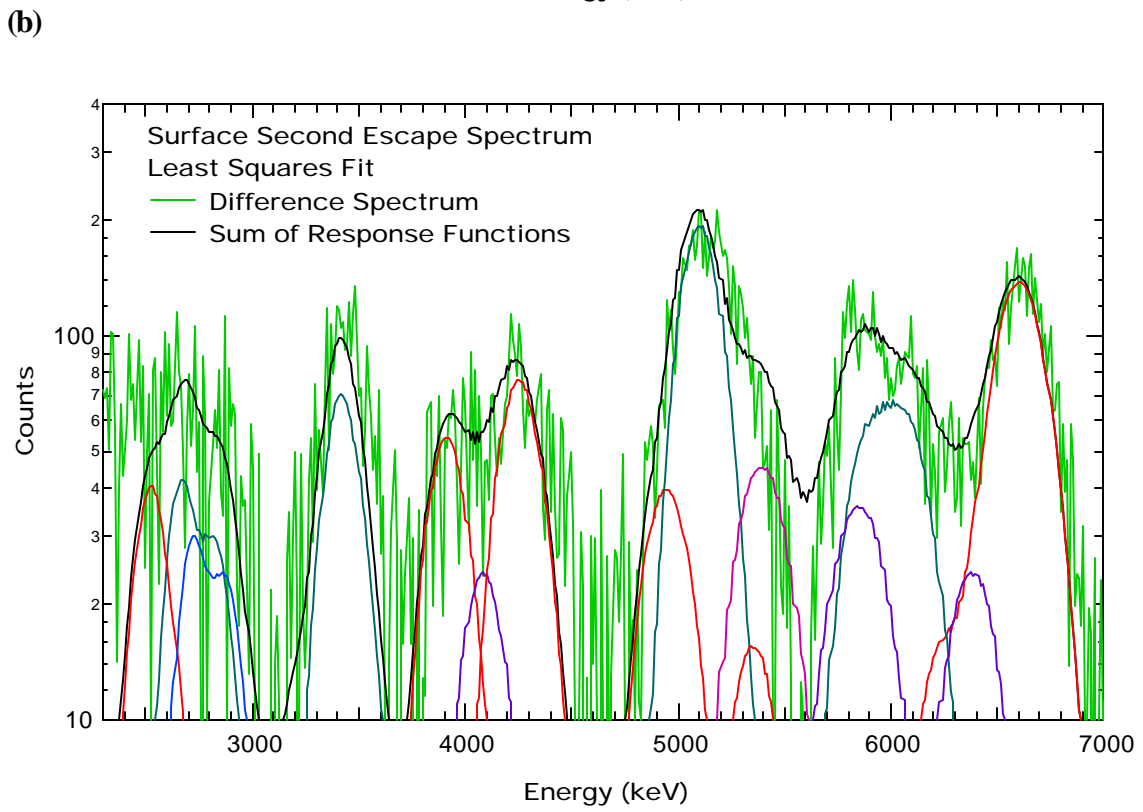
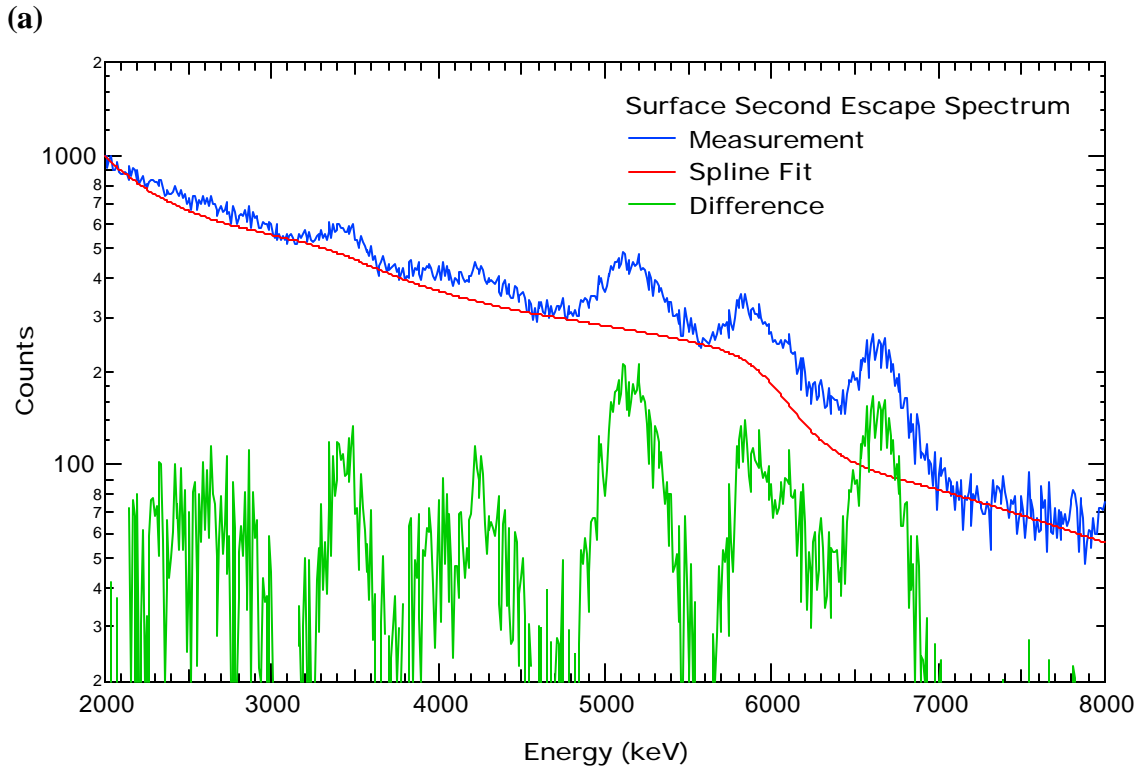


Figure 9.

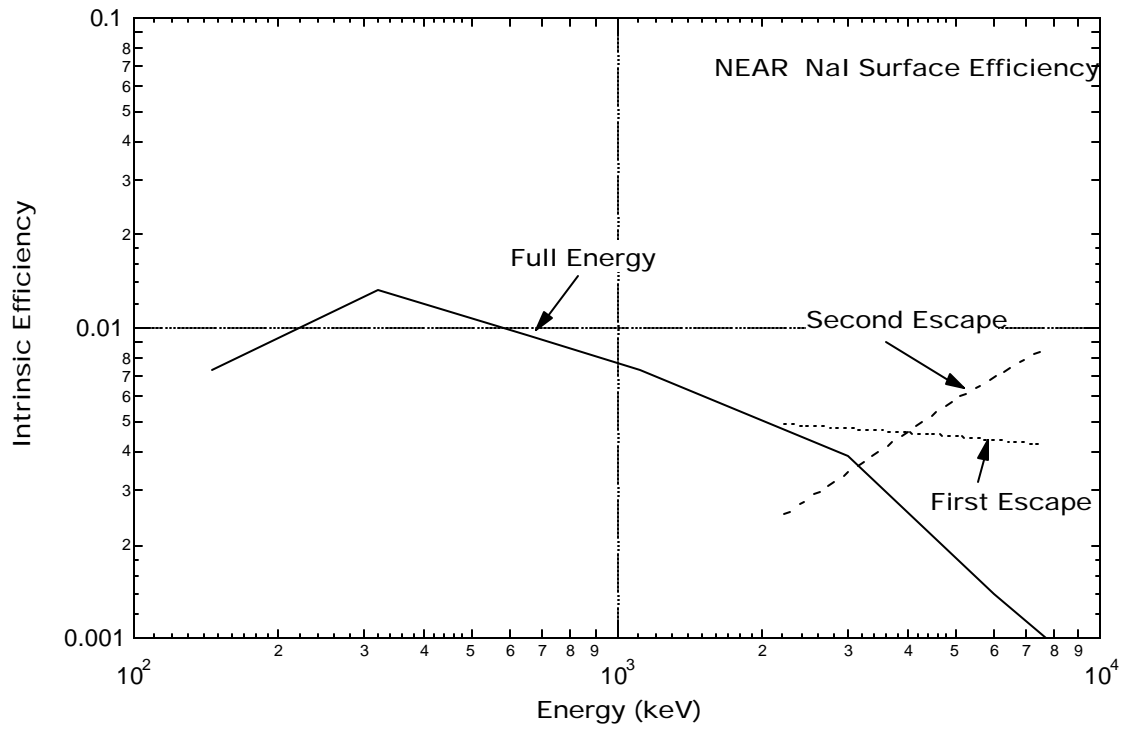
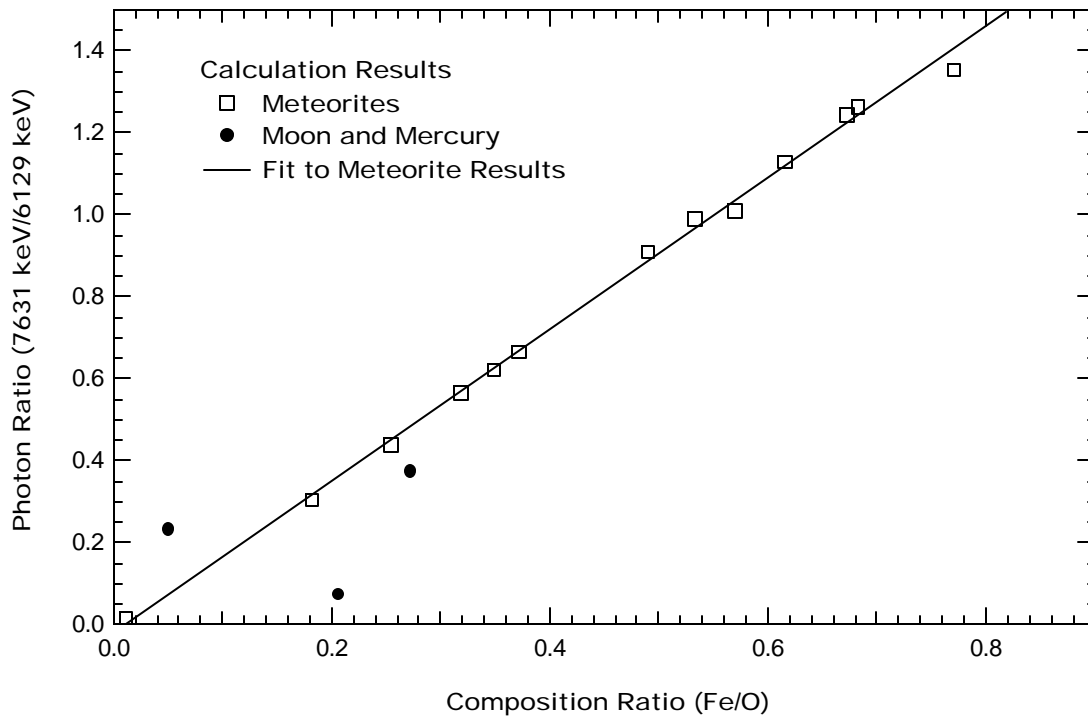


Figure 10.

(a)



(b)

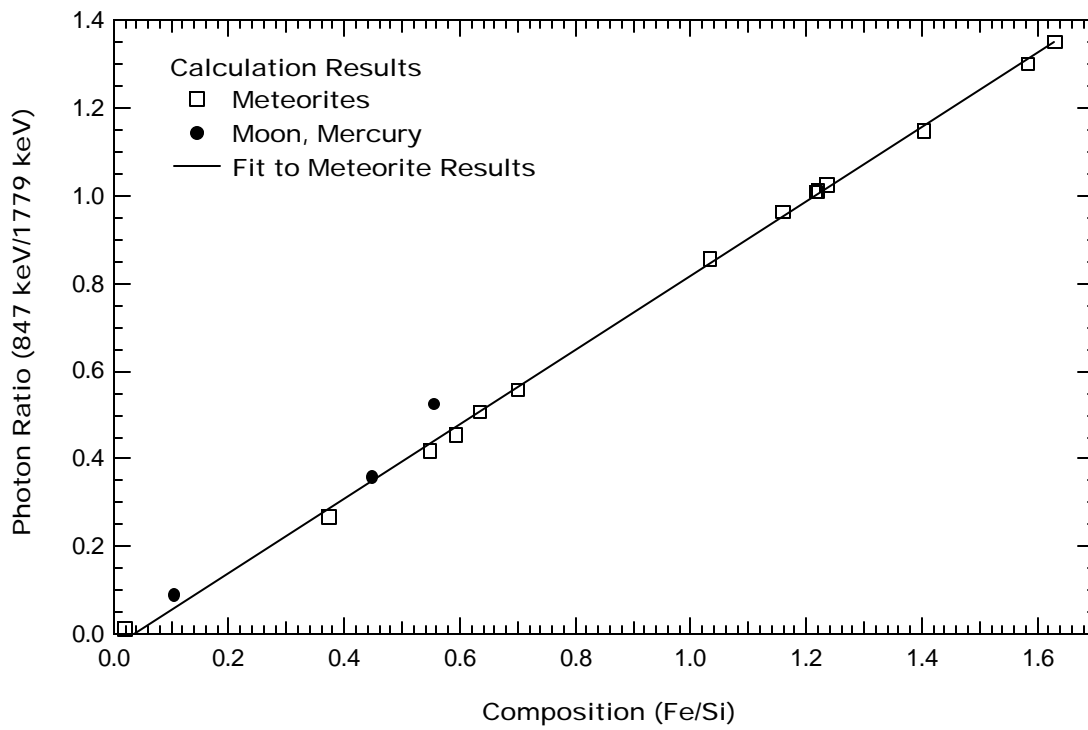


Figure 11.

